AGU PUBLICATIONS

Water Resources Research

RESEARCH ARTICLE
10.1002/2017WR021153

Key Points:
- Large capillary pressures, on the order of 1 MPa, can be required to desaturate shales
- Water vapor adsorption in shales is strongly diffusion-limited
- New conceptual model reconciles strong water blocking and high rates of gas production in hydraulically fractured unconventional reservoirs

Correspondence to:
T. K. Tokunaga,
tktokunaga@lbl.gov

Citation:
Tokunaga, T. K., Shen, W., Wan, J., Kim, Y., Cihan, A., Zhang, Y., & Finsterle, S. (2017). Water saturation relations and their diffusion-limited equilibration in gas shale: Implications for gas flow in unconventional reservoirs. *Water Resources Research*, *53*. https://doi.org/10.1002/2017WR021153

Received 22 MAY 2017
Accepted 11 NOV 2017
Accepted article online 15 NOV 2017

Water Saturation Relations and Their Diffusion-Limited Equilibration in Gas Shale: Implications for Gas Flow in Unconventional Reservoirs

Tetsu K. Tokunaga[1], Weijun Shen[2,3], Jiamin Wan[1], Yongman Kim[1], Abdullah Cihan[1], Yingqi Zhang[1], and Stefan Finsterle[1]

[1]Lawrence Berkeley National Laboratory, Energy Geosciences Division, Berkeley, CA, USA, [2]Key Laboratory for Mechanics in Fluid Solid Coupling Systems, Institute of Mechanics, Chinese Academy of Sciences, Beijing, China, [3]Institute of Mechanics, University of Chinese Academy of Sciences, Beijing, China

Abstract Large volumes of water are used for hydraulic fracturing of low permeability shale reservoirs to stimulate gas production, with most of the water remaining unrecovered and distributed in a poorly understood manner within stimulated regions. Because water partitioning into shale pores controls gas release, we measured the water saturation dependence on relative humidity (*rh*) and capillary pressure (P_c) for imbibition (adsorption) as well as drainage (desorption) on samples of Woodford Shale. Experiments and modeling of water vapor adsorption into shale laminae at $rh = 0.31$ demonstrated that long times are needed to characterize equilibrium in larger (5 mm thick) pieces of shales, and yielded effective diffusion coefficients from 9×10^{-9} to 3×10^{-8} $m^2\ s^{-1}$, similar in magnitude to the literature values for typical low porosity and low permeability rocks. Most of the experiments, conducted at 50°C on crushed shale grains in order to facilitate rapid equilibration, showed significant saturation hysteresis, and that very large P_c (~1 MPa) are required to drain the shales. These results quantify the severity of the water blocking problem, and suggest that gas production from unconventional reservoirs is largely associated with stimulated regions that have had little or no exposure to injected water. Gravity drainage of water from fractures residing above horizontal wells reconciles gas production in the presence of largely unrecovered injected water, and is discussed in the broader context of unsaturated flow in fractures.

Plain Language Summary Large volumes of water are used for hydraulic fracturing of low permeability shale reservoirs to stimulate gas production. While most of the water remains unrecovered, gas production is commonly surprisingly high, despite blocking of gas flow by water. In order to understand the energetics of water saturation, we measured saturation dependence on water potential in samples of Woodford Shale. Experiments and modeling of water vapor diffusion into 5 mm thick shale laminae yielded effective diffusion coefficients similar in magnitude to the literature values for typical low porosity and low permeability rocks. Most of the experiments showed significant saturation hysteresis, and that very large capillary pressure (~1 MPa) are required to drain the shales. These results quantify the severity of the water-blocking problem, and suggest that gas production from unconventional reservoirs is largely associated with stimulated regions that have had little or no exposure to injected water. A conceptual model based on gravity drainage of water from fractures residing above horizontal wells is discussed that reconciles gas production despite the large volumes of unrecovered injected water. Thus, the potential advantages of waterless hydraulic fracturing techniques in improving gas production are further supported.

1. Introduction

The injection of water for hydraulic fracturing of deep, low permeability "unconventional" shale reservoirs has proven surprisingly effective for the extraction of natural gas (Alexander et al., 2011). However, the large volumes of water consumed, the hazardous chemical composition of produced water (the combination of injected water and native formation water recovered in the return flow requiring proper treatment and disposal), and the high cost of wastewater treatment have attracted considerable public concern and regulatory oversight (EPA, 2016; Vengosh et al., 2014). Relatively less attention has been given to the nature of

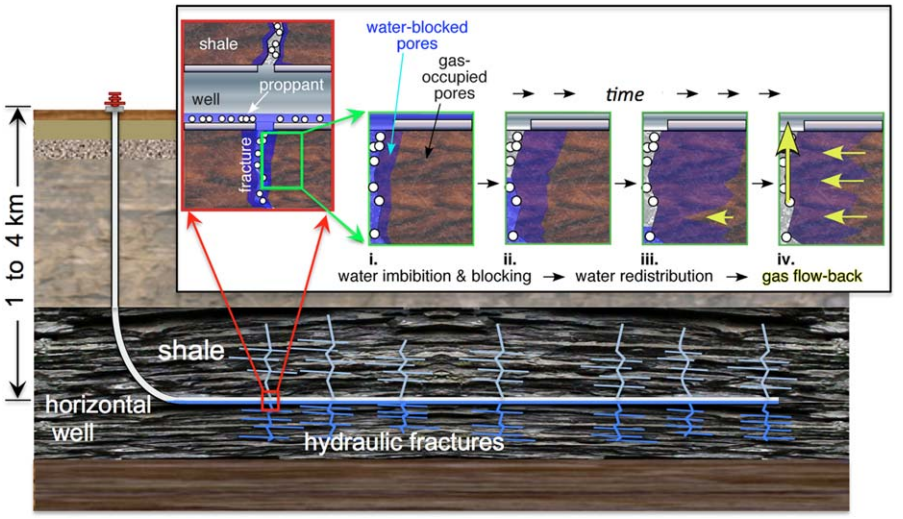

Figure 1. Conceptual illustration of hydraulic fractures generated from horizontal wells in a shale gas reservoir. Fractures residing above the horizontal well are hypothesized to drain quickly, thus are only weakly affected by water blocking and facilitate early gas production. Fractures residing below the horizontal well are hypothesized to drain slowly, such that gas production becomes possible as the water level declines in the fracture, primarily through imbibition into the shale matrix. The insert depicts the time-dependent localized distribution of injected water along fracture-shale matrix interfaces following hydraulic fracturing, along with declining water level in a fracture below the horizontal well. Note that counterflow (counter-current imbibition) of gas to the well through redistribution of imbibed water is hypothesized to be significant only in regions adjacent to drained portions of fractures.

water retained in shale reservoirs. With over a million gallons of water typically injected to develop the average unconventional gas well (Gallegos et al., 2015), and less than 30% of this water usually recovered (Birdsell et al., 2015; Clark et al., 2013; Singh, 2016), water retention in shale is clearly very important. Moreover, the immiscibility of water and gas underlies the detrimental influence of water in shale matrix pores, water blocking of gas flow (Bertoncello et al., 2014; Kamath & Laroche, 2003; Yan et al., 2015) to fractures and wells (Figure 1). Indeed, the negative aspects of water-based hydraulic fracturing (use of large volumes of water, required treatment of flowback water, and water blocking of gas flow) continue to stimulate interest in developing fracturing fluids containing little or no water. These alternative fracturing fluids include CO_2, N_2, hydrocarbons, and their foams in order to reduce water consumption in unconventional shale reservoirs (Gupta, 2009; Gupta & Bobier, 1998; Liu et al., 2014; Wanniarachchi et al., 2017; Xue et al., 2016).

While water blocking of gas flow back into fractures is well recognized (Bennion & Thomas, 2005; Holditch, 1979; Spencer, 1989), relatively little is known about the energy status of water in the shale matrix responsible for resisting water drainage. The energetics of adsorptive and capillary retention of water in partially saturated shales needs to be investigated because water blocking reflects the strength of these forces, and because of the dominant influence of water on gas relative permeability. Indeed, the commonly observed coexistence of very low relative permeabilities to both gas and water at intermediate saturations (referred to as the "permeability jail" phenomenon) reflects the strength of adsorptive and capillary retention of water (Engelder et al., 2014; Spencer, 1989). Because of the very fine pore sizes characteristic of shales (Clarkson et al., 2013; Nelson, 2009), partially saturated conditions are associated with low water activity (low relative humidity), very low water potentials, and very strong capillary pressures. Although water-gas capillary pressure relations have been inferred from mercury intrusion porosimetry, variable reliability of such predictions is attributable to uncertainties associated with wettability (Busch & Amann-Hildenbrand, 2013).

Despite the importance of water saturation in restricting gas flow through shales, relatively few direct measurements of shale water saturation as a function of water potential have been reported. In some studies, shales have been equilibrated in controlled relative humidity (*rh*) environments in order to obtain water vapor adsorption isotherms (Chenevert, 1970; Dosunmu & Okoro, 2012; Li et al., 2016; Seemann et al., 2017) that are beyond the range achievable with experimental techniques based on controlling differential

pressures. An equivalent approach involves adjusting water contents of shales to specific levels and measuring the associated equilibrium *rh* values (Donnelly et al., 2016; Ferrari et al., 2014).

In order to quantify the potential energy levels associated with water blocks in shales, it is particularly important to measure drainage (desorption) isotherms that have closer correspondence to gas breakthrough capillary pressures. In our search of the literature, very few previous studies have reported desorption isotherms, and their conclusions are inconsistent. A couple of studies have reported significant hysteresis in adsorption and desorption isotherms (Chenevert, 1970; Ferrari et al., 2014), while another recent study reported negligible hysteresis (Donnelly et al., 2016). Moreover, to our knowledge, no previous study utilized a combination of humidity and capillary pressure control methods in order to examine the full range of water retention relations. Given the importance of both water imbibition and drainage, and the commonly hysteretic nature of moisture retention in porous media, our present study is focused on both of these processes. Unlike these previous studies that were all conducted at room temperature, most experiments presented here were performed at 50°C, a compromise between experimental convenience and the higher temperatures associated with deep shale formations. These measurements were performed on Woodford Shale, an important Late Devonian to Early Mississippian gas and oil source rock occurring in Oklahoma, regarded as one of the seven major North American gas shale plays (Cardott, 2012). In addition, transient water vapor adsorption was investigated at one relative humidity condition in order to examine the time dependence of vapor phase transport and equilibration in shale. The vapor adsorption process was analyzed numerically in order to quantify effective water vapor diffusion coefficients under relatively dry conditions. This latter experiment and numerical analysis helps elucidate times required to reach equilibrium in laboratory measurements, particularly important in tests of larger rock pieces.

The collective results provide understanding on the strength of capillary and adsorptive retention of water in shales, and underscore the severity of water blocking in restricting return flow of gas. Recognizing water blocking, the loss of most of the injected water in and around newly generated fractures in unconventional reservoirs appear at odds with commonly encountered high gas productivity. We conclude with a conceptual model of water distribution that reconciles this apparent disparity.

2. Materials and Methods

2.1. Shale Samples and Their Chemical-Physical Characterization

Woodford Shale samples from five different locations within this formation were obtained from the Oklahoma Geological Survey (http://www.ogs.ou.edu/level3-OPICcorefacility.php). Origins of these samples are listed in Table 1 along with abbreviated sample labels. Characterization methods applied to these samples have included elemental analyses by X-ray fluorescence (XRF), organic and inorganic carbon analyses, mineralogy (X-ray diffraction, XRD), scanning electron microscopy (SEM), densities, porosities, and specific surface area measurements. The < 250 μm fraction of crushed shale was further milled to < 10 μm in order to be used for the XRF (Orbis, EDAX), organic and inorganic carbon analyses, and XRD measurements. Major mineral composition of the Woodford shale samples was determined by X-ray diffraction (Rigaku Smartlab, CuK_{α} source at 40 kV, 35 mA) using the American Mineralogist Crystal Structure Database (Downs & Hall-Wallace, 2003).

For obtaining SEM images, polished thin sections, 30 μm thick and 25 mm diameter, of the Woodford shale samples were prepared by a commercial petrographic service (Burnham Petrographic, LLC). The thin section surfaces originally contained some volatile organic carbon (organic droplets observed under the light

Table 1
*Woodford Shale Samples Obtained From the Oklahoma Geological Survey (*OGS)*

County	OGS* #	LBNL label	Well	Sample depth (m)
Custer, OK	956	WHf	Hoffman	4346.3–4347.2
Blaine, OK	482	WR	Roetzal	2569.0–2569.9
Wagoner, OK	4599	WD	Dunkin	282.3–283.1
Okfuskee, OK	2595	WH1	Holt	1126.7–1127.6
Okfuskee, OK	2595	WH2	Holt	1128.5–1129.4

microscope). Therefore, before the gold coating preparation for SEM analyses, the surficial organic droplets were removed using solvent (acetone). The thin sections were sputter coated with a thin layer (10 nm) of gold to increase the surface conductivity. The SEM (Zeiss, Gemini Ultra-55) images were taken with a back-scattered electron detector.

Given the importance of surface area on water adsorption and capillarity, specific surface areas of crushed shale samples were obtained using different gases, as well as water vapor. N_2 and Kr were used as adsorbates for determining specific surface area with the Brunauer-Emmett-Teller (BET) method (Brunauer et al., 1938) with an Autosorb-1 (Quantachrome), in our laboratory as well as at Particle Technology Labs (Downers Grove, IL). Water vapor adsorption data from the low range in adsorption isotherms were also used to estimate BET surface areas.

2.2. Water Vapor Adsorption and Desorption Isotherms

In order to expedite reaching adsorption and desorption equilibrium while maintaining micropore structure, larger chips of the Woodford samples listed in Table 1 were crushed and sieved to select grain-size ranges of 500–800 μm and 250–500 μm. For brevity, these will be referred to as 700 and 350 μm grains, respectively. The 700 and 350 μm grain-size samples of each shale were first oven-dried at 105°C (24 h), then cooled to room temperature in a vacuum desiccator, and weighed to establish the dry mass. Samples were then equilibrated at progressively higher water vapor pressures in desiccators containing saturated salt solutions (Tokunaga et al., 2003), incubated at 50°C. This temperature was selected as a compromise between the convenience of room temperature experiments (to the best of our knowledge, used in all previous water vapor adsorption isotherms for shales), and temperatures in deep reservoirs that approach and even exceed 100°C. Individual samples were contained in glass weighing bottles left open while in desiccators, and immediately sealed when removed for weighing. Water vapor pressures within desiccators were regulated using saturated salt solutions that provide fixed relative humidities (Greenspan, 1977). These salts and relative humidities, *rh*, are listed in Table 2, along with their associated water potentials Ψ, and Kelvin pore radii, *r*. Water potentials were calculated from

$$\Psi = \left(\frac{\rho_w RT}{M_w}\right) \ln(rh) \tag{1}$$

where ρ_w is the density of water, R is the gas constant, T is the Kelvin temperature, and M_w is the molar mass of water. Note that values of Ψ are of large magnitude (MPa) and negative. Although $-\Psi$ is often assumed to be equal to the capillary pressure P_c, the solute (or osmotic) contribution to Ψ can amount to a few MPa in shales because of highly saline pore waters, thus lowering the magnitude of P_c. More generally, Ψ as expressed in equation (1) is simply the chemical potential multiplied by the density of water, rather than a mechanical pressure (Sposito, 1981). Rearranging the Kelvin equation gives the equivalent pore radius

$$r = \frac{-2\gamma M_w}{\rho_w RT \ln(rh)} \tag{2}$$

where γ is the water-air interfacial tension. Equation (2) will be useful for estimating pore sizes where water condensation occurs at specific *rh* levels.

After reaching adsorption equilibrium at the highest $rh = 0.96$, samples were transferred to the pressure plate device for measuring water retention behavior at higher levels of saturation. After completion of the pressure plate imbibition-drainage cycle, samples were returned to the saturated salt-controlled environments to undergo progressive desorption from $rh = 0.96$ down to 0.11.

Table 2
Relative Humidities for Equilibrating Shale Samples (50 °C), Controlled by Saturated Salt Solutions, and Associated Water Potentials and Kelvin Radii

	Salt	LiCl	$MgCl_2$	NaBr	$NaNO_3$	KBr	KCl	KNO_3	K_2SO_4
rh (at 50°C)		0.11	0.31	0.51	0.70	0.79	0.81	0.85	0.96
Water potential	MPa	−328	−177	−100	−53	−35	−31	−25	−6
Kelvin radius (*r*)	nm	0.4	0.8	1.4	2.6	3.9	4.4	5.5	21

2.3. Diffusion-Limited Water Vapor Adsorption

Time scales required to achieve vapor adsorption equilibrium also need to be understood. Although vapor adsorption into the 700 and 350 μm shale grains is intrinsically diffusion limited, the gravimetric measurements of water uptake in these small grain sizes did not allow the highly time resolved measurements needed to quantify diffusion rates. This process will be developed further in future work, but to illustrate the importance of transport limitations, some larger pieces of Woodford Shale were sliced along bedding planes into nominally 5 mm thick laminae for experimental and computational examination of diffusion-limited water vapor adsorption.

2.3.1. Experimental

The experimental procedure was similar to that used with the shale grains, with the exception that the thicker shale slices were used for measuring moisture uptake from initially dry states up to equilibrium at $rh = 0.31$. The characteristic dimensions of the shale slices are indicated in Table 3.

2.3.2. Modeling

We employed both numerical and analytical modeling approaches to estimate the magnitudes of the effective diffusion coefficients in the shale laminae (Table 3) and assess major diffusive transport processes. The numerical model is based on solution of the Maxwell-Stefan diffusion equations for a binary mixture of water and air, including Knudsen diffusion and adsorption. Surface diffusion of water along pore walls may also be important (Krishna & Wesselingh, 1997), but its separate evaluation is beyond the scope of this study. In the continuum limit, where the mean free path of gas phase molecular collisions (l_o) is small relative to the characteristic pore radius (r_o), the diffusion coefficient for water vapor through air is taken as the product of a gas porosity-dependent factor $f(\varepsilon)$ times the binary molecular diffusion coefficient in the bulk gas phase denoted by D_o. The Knudsen contribution accounts for the influence of vapor phase water molecule collisions with pore walls (Loeb, 1961; Wesselingh & Krishna, 2000), with its diffusion coefficient is denoted by D_K. In the analytical model, Maxwell-Stefan diffusion effects considering interaction between different molecule types are ignored, and Fickian diffusion is assumed. In that case, the effective diffusion coefficient can be given as

$$\frac{1}{D_{eff}} = \frac{1}{f(\varepsilon)D_o} + \frac{1}{D_K} \tag{3a}$$

or equivalently

$$D_{eff} = \frac{f(\varepsilon)D_o}{1 + Kn} \tag{3b}$$

which are forms of Bosanquet's equation for gas diffusion in porous media, accounting for Knudsen effects (Pollard & Present, 1948; Tokunaga, 1985). In equation (3b), $Kn = l_o/r_o$ denotes the Knudsen number, i.e., the ratio of the gas mean free path to the characteristic pore radius (r_o). For H_2O diffusing through a gas phase consisting primarily of N_2 (78%) and O_2 (21%), an estimated collision diameter $\sigma = 0.31$ nm was obtained from averaging of kinetic diameters (Li et al., 2009; Loeb, 1961; Massman, 1998). The mean free path for H_2O vapor diffusion in air was then estimated from kinetic theory (Loeb, 1961) as

$$l_o = \frac{k_B T}{\sqrt{2}\pi\sigma^2 P} \tag{4}$$

which at 50°C and local atmospheric pressure (98 kPa) gives $l_o = 110$ nm.

For the numerical model, we used COMSOL Multiphysics Software tool, and for the analytical model we employed a computer code to evaluate the analytical solution for the diffusion and the linear adsorption in

Table 3
Woodford Shale Samples for Quantifying Diffusion-Limited Adsorption

LBNL label	Porosity	Thickness	Length (mm)	Width
WR	0.081	5.1 ± 0.9	20.9 ± 3.0	11.8 ± 1.6
WD	0.106	5.2 ± 0.4	23.8 ± 0.8	12.3 ± 0.7
WH1	0.063	5.6 ± 0.2	23.5 ± 1.4	13.1 ± 1.1

Note. Dimensions of samples are averages of five pieces (± standard deviations).

a rectangular parallelepiped domain given by Ozisik (1980) in the heat transfer context. Based on our model comparisons using the same input parameters, the differences between the more general numerical model and the analytical model are negligible. Therefore we selected the analytical model to conduct inverse modeling analyses using iTOUGH2-PEST (Finsterle & Zhang, 2011) to estimate the magnitude of the effective diffusion coefficient and the distribution coefficient for the linear adsorption. For the low value of the relative humidity in the measurements ($rh = 0.31$), a linear adsorption model can be used to represent the adsorption of water molecules on solid surfaces of the shale matrix, as $C_s = K_d \times C_{H2O}$, where C_s is the mass of adsorbed water per unit mass of the shale (kg kg^{-1}), K_d is the distribution coefficient (m^3 kg^{-1}), and C_{H2O} is the mass of water vapor per unit volume of the gas phase (kg m^{-3}). The selection of linear or nonlinear adsorption models at $rh = 0.31$ would have minimal impact on the final estimated value of the diffusion coefficient. In the model simulations, we assumed the water vapor concentration in all the shale rock blocks is initially zero and at times greater than zero the water vapor concentration along all the sides of the samples are kept at $rh = 0.31$ under isothermal conditions (T = 50°C), as in the experiments.

2.4. Pressure Plate Imbibition-Drainage Curves

At $rh > 0.96$, accurate control of Ψ through the vapor phase becomes impractical because of increased sensitivity to water condensation resulting from small temperature variations. The pressure plate method is well suited for directly controlling P_c in this extremely high rh region, via controlling pressure differences above and below a porous ceramic plate (Dane & Hopmans, 2002). We used a 500 kPa pressure plate in a 500 kPa chamber (Soilmoisture Equipment Corp.), housed in an incubator maintained at 50 ± 0.5°C (Figure 2). Compressed air was supplied to the chamber via a two-stage pressure regulator, controlling P_c to within 1 kPa. A 1.0 *M* KCl solution was used to saturate the porous plate, and as the high ionic strength imbibing/draining solution for the shales. An open container of 1.0 *M* KCl was included in the pressure chamber in order to assure maintenance of $rh \sim 1$. The outflow tube from the pressure plate led into the bottom of an outflow reservoir containing the same solution, and having its free surface of this reservoir kept at about 1 cm below the level of the pressure plate. This configuration allowed use of the pressure plate in both imbibition and drainage processes.

After shale samples reached vapor adsorption equilibrium at the highest applied $rh = 0.96$, they were transferred to 54 mm I.D. stainless steel sample rings for pressure plate equilibrations. Each sample ring was lined with a sheet of filter paper (Whatman 4), supported with linen gauze, and tightly secured to the ring with Kapton tape. When distributed onto the filter paper base of the sample rings, the thickness of the crushed shale pack was about 3 mm. The sample rings were placed onto the pressure plate, and the chamber pressure was raised to specific target P_c values. Moisture uptake and release from shale samples was monitored through periodically depressurizing the chamber and weighting sample rings as well as duplicate "blank" rings (taped, filter paper, and gauze support). The three P_c values applied were 450, 100, and 30 kPa, and required equilibration times ranged from 6 to 21 days. No lower magnitude P_c levels were tested because they would have included progressively more significant contributions of pendular water at contact points between the loose grains. Upon reaching drainage equilibrium at 450 kPa, samples were returned to the $rh = 0.96$ chamber to initiate the series vapor desorption steps.

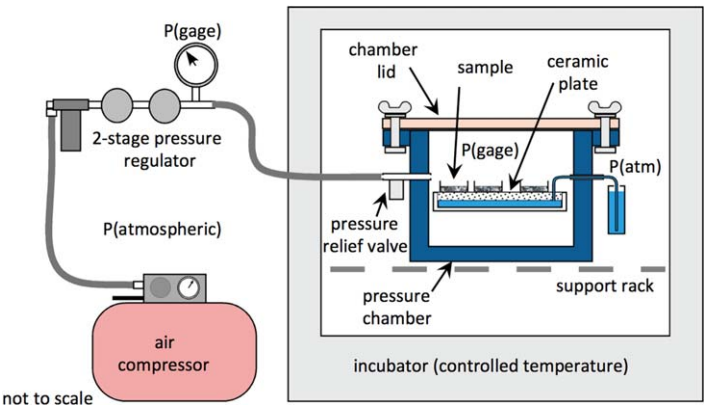

Figure 2. Pressure plate system for measuring imbibition and drainage on shale samples at moderately elevated temperature (50°C).

3. Results and Discussion

3.1. Shale Characterization

The XRF analyses (Table 3) yielded elemental compositions from the five shale samples that were similar with the exception of WH1, which had a high concentration of Ca (11.7% mass). Total organic carbon (TOC) values ranged from 2.7% to 7.1% (mass basis). High concentrations of total inorganic carbon (TIC = 3.6%) were found in only one sample, WH1, and the XRD analyses confirmed the presence of calcite in this sample. Quartz and illite are the minerals common to all samples, although the relative abundance of illite in these samples is likely to be low, based on surface area measurements described later. Previous studies of Woodford Shale have characterized it as brittle, with only low amounts of swelling clays (Cardott, 2012; Clarkson et al., 2013). It is

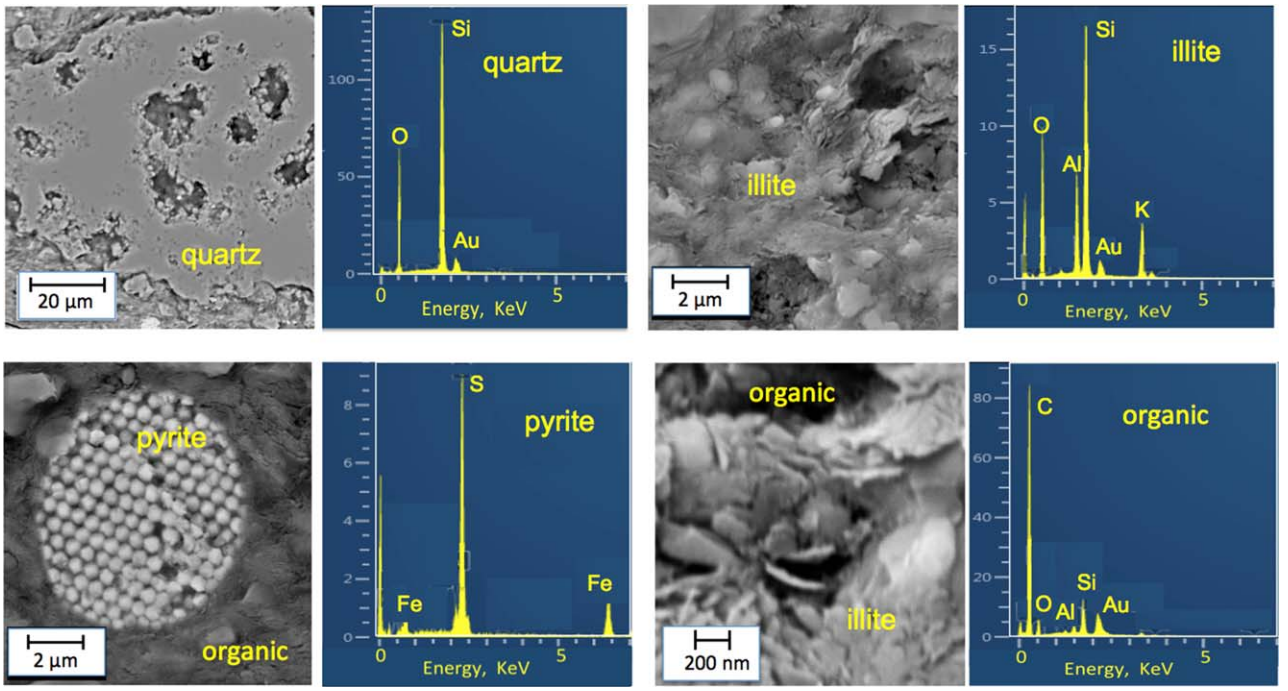

Figure 3. Characteristic SEM images from Woodford samples WR and WD, and associated EDS; Si and O-rich quartz region; Si, Al, O, K-rich illite region, Fe and S-rich pyrite, and C-rich organic region (Au in all spectra are from sputter coating).

worth mentioning here that swelling and disaggregation observed on some shales (Dehghanpour et al., 2013; Schmitt et al., 1994) was not evident during wetting of samples, consistent with this mineralogy, as well as with the use of 1 M KCl for bringing shales up to highest saturations.

SEM images show complex micromorphology typical of shales, with a few representative images presented in Figure 3. The compositions from energy dispersive spectrometer spot analyses showing dominant elements consistent with dominant minerals identified through bulk XRD and inferred from XRF; illite, quartz, pyrite, as well as organic/kerogen-rich inclusions. Complex pore geometries, with pore sizes from tens of nanometer to several micrometers, were characteristic of all samples.

The N_2 and Kr BET analyses from both laboratories yielded very low specific surface areas, ranging from 0.21 to 3.0 $m^2\ g^{-1}$ (Table 4). With the exception of the calcite-rich WH1 sample, all surface areas obtained with N_2 or Kr BET analyses are less than 1.0 $m^2\ g^{-1}$. In contrast, others have typically obtained higher BET-specific surface areas for shale samples. For example, Clarkson et al. (2013) analyzed a variety of shales, and reported N_2 BET surface areas ranging from 2 up to 17 $m^2\ g^{-1}$, with Woodford Shale samples yielding values of about 2.4 and 7.4 $m^2\ g^{-1}$. Devonian-Mississippian shales analyzed by Ross and Bustin had N_2 BET surface areas ranging from 2 to 17 $m^2\ g^{-1}$, with Woodford Shale samples yielding values of about 3.4 and

Table 4
Elemental Composition of Woodford Shales (XRF Values Are Not Reported as Oxides, and TIC/TOC)

LBN label	%											Major minerals
	Al	Si	P	S	K	Ca	Ti	Mn	Fe	TIC	TOC	
WHf	9.1	32	0.1	0.3	3.5	1.2	0.4	0.09	3.1	0.40	3.89	q, il[a]
WR	6.6	32	0.1	0.9	3.3	1.0	0.3	0.04	2.0	0.00	7.11	q, il[a]
WD	8.6	30	0.1	0.3	4.3	1.3	0.3	0.03	3.0	0.46	5.61	q, il[a]
WH1	4.8	22	0.1	0.1	1.8	12	0.2	0.01	1.0	3.61	2.68	q, il[a], c
WH2	10	28	0.2	0.2	5.2	2.4	0.5	0.02	2.1	0.00	5.54	q, il[a]

Note. Major mineralogy determined by XRD; q = quartz, il = illite, c = calcite (12 ± 2%).
[a]Illite abundance is likely < 5%, based on low values obtained for specific surface areas.

Table 5
Surface Areas of Woodford Shale Samples Obtained With N_2, Kr, and H_2O BET Analyses

		$m^2\ g^{-1}$			
LBNL label	Porosity	BET (N_2)	BET (Kr)	BET (H_2O 30°C)	BET (H_2O 50°C)
WHf	0.065	0.21	0.27	14	18
WR	0.081	0.24	0.29	16	18
WD	0.106	0.31		14	15
WH1	0.063	3.03		8.5	8.7
WH2	0.067	0.91		15	17

Note. Relative uncertainties in BET surface areas are ~10% with N_2 and Kr, and ~15% with H_2O.

44.5 $m^2\ g^{-1}$ (Ross & Bustin, 2009). Kuila and Prasad obtained N_2 BET surface areas ranging from 0.98 to 31.8 $m^2\ g^{-1}$ for various shales, including a Woodford Shale sample with a value of 1.93 $m^2\ g^{-1}$ (Kuila & Prasad, 2013).

We also applied the BET analysis directly to water vapor adsorption data to obtain alternate estimates of specific surface area (Tokunaga et al., 2003). However, it should be noted that H_2O-based analyses are known to overestimate surface areas in systems where ion hydration is significant (Quirk, 1955). Given that only the two lowest water vapor adsorption data points ($rh = 0.11$ and 0.31) were used for the H_2O-based BET analyses, with the higher value at the upper limit ($rh \sim 0.3$) of expected linearity (Rouquerol et al., 1994), this procedure has high uncertainty. Applying the BET method with water vapor data, we obtained specific surface areas more consistent with the measured water uptake, mostly ranging from 13 to 18 $m^2\ g^{-1}$, with the WH1 being distinctly lower (~8.6 $m^2\ g^{-1}$). Although these values are more consistent with the water uptake data, they do not constitute independent measurements because they are calculated from the water vapor adsorption results. Given likely ion hydration influences, specific surface values are expected to be lower than those obtained by H_2O-BET.

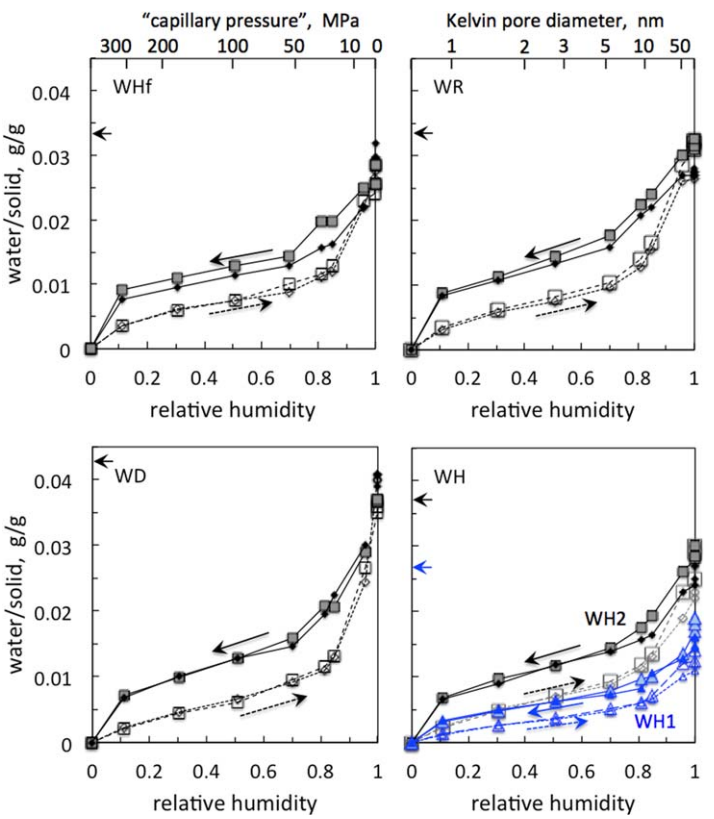

Figure 4. Adsorption and desorption isotherms for Woodford Shales at 50°C. Refer to Table 1 for identifying characteristic of the individual samples. The 350 and 750 μm grain-size samples are indicated by smaller and larger data points, respectively. Adsorption and desorption paths are indicated with arrows along curves. Water:solid mass ratios corresponding to full saturation are indicated by arrows on the y axes.

The complex interactions between adsorbent (substrate) and adsorbate are also evident upon examining specific surface areas obtained for the calcite-rich WH1 shale. Among the surface areas obtained with N_2 (Table 5), the value for WH1 is distinctly higher than that of the other shales, and consistent with its higher porosity (Table 3). Conversely, when water is used as the adsorbate, surface areas for WH1 are distinctly lower than for the other Woodford Shales, suggesting that the lower wettability of calcite influences the result. More broadly, the inconsistencies partly reflect the fact that specific surface areas of geological materials are measurement method-dependent parameters rather than fundamental material properties (Sposito, 1984).

3.2. Water Vapor Adsorption/Desorption Isotherms and Imbibition/Drainage Curves

Results of the combined water vapor adsorption/desorption isotherms and imbibition/drainage curves at 50°C are shown in Figure 4. The adsorption and desorption isotherms are presented in terms of variations in water:solid mass ratios (mass of water per unit mass of oven-dry shale) with respect to *rh*. Relative uncertainties in water contents are all less than 0.05, while uncertainties in *rh* are all less than 0.01. Water contents corresponding to full saturation (based on measured densities and porosities) are indicated by arrows along the *y* axes. Note that the curves from the 700 and 350 μm grain-size fractions of each shale sample were generally very similar, indicating that

intragranular porosity and pore-size distributions were identical. These data clearly show hysteresis characteristic of equilibrium states of water in porous media, and show that substantial decreases in *rh* are required for removing water from the shale matrix. It is worth noting that these curves mostly show similar magnitudes of moisture retention at any given path-specific *rh*. The exceptions are associated with the WH1 samples that have substantially lower water contents. WH1 was the only sample containing significant concentrations of inorganic carbon as calcite (3.61 mass % of C, 11.7 mass % Ca, Table 3), consistent with less hydrophilic characteristics of carbonate surfaces (Elgmati et al., 2011; Morrow, 1990; Roychaudhuri et al., 2013). Equivalent capillary pressures based on either equation (1) or pressure differentials applied with the pressure plate method are provided along the upper *x* axis of the WHf isotherms. Also plotted on these graphs are results from the pressure plate measurements, although difficult to visualize here because they are associated with $rh > 0.99$.

It is important to note that increased saturation measured with increased *rh* and decreased P_c does not strictly allow predictions of pore size based on application of physicochemical principles to simple geometric surface and pore models. Physisorption of condensing fluids often follows the BET model at low vapor pressures, thus justifying its routine use for surface area measurements. However, as mentioned earlier, water vapor adsorption is enhanced through hydration of surface ions, thus overestimates surface area in materials having significant cation exchange capacity (Quirk, 1955). The validity of the Kelvin equation has been demonstrated in axisymmetric systems down to interfacial radii as low as 4 nm (Fisher & Israelachvili, 1979; Mitropoulos, 2008). However, complex pore network geometries of geological media are only approximated with equivalent pore sizes. Moreover, the converging and diverging pore cross-sections generally lead to entrapment of the nonwetting phase and slow equilibration. Such irregular pore geometries combined with uncertain contact angles prevent assignment of unique relations between *rh* and pore size (Seemann et al., 2017; Sing & Williams, 2004). With these caveats in mind, *rh*-estimated sizes of pores filling (and draining) were taken as twice the Kelvin radius (Equation 2), and indicated along the upper *x* axis for plots of the WR isotherms (Figure 4). The data collectively indicate that equivalent diameters of most of the pores are in the 1 to ~20 nm range.

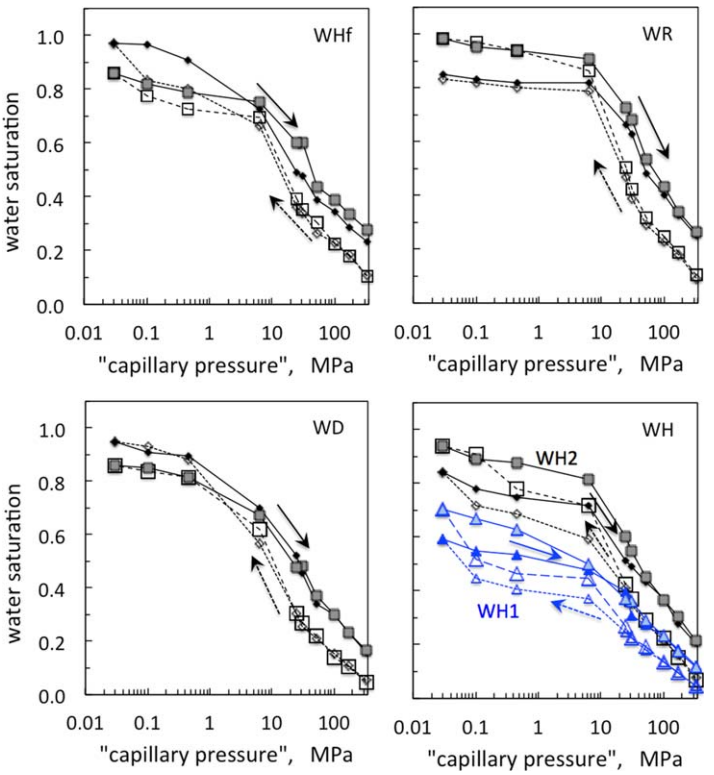

Figure 5. Adsorption and desorption isotherms for Woodford Shales at 50°C, presented in terms of equivalent P_c. Refer to Table 1 for identifying characteristic of the individual samples. The 350 and 750 μm grain-size samples are indicated by smaller and larger data points, respectively. Adsorption (imbibition) and desorption (drainage) paths are indicated with arrows along curves, respectively. Water:solid mass ratios corresponding to full saturation are indicated on the y axes.

The water adsorption-desorption relations are plotted in terms of the water saturation dependence on the capillary pressure in Figure 5. For purposes of assessing water blocking, this representation of saturation relations is more informative than the plots with respect to *rh* because magnitudes of P_c required to significantly desaturate shales are directly presented. As noted previously, equation (1) was used to convert *rh* to Ψ for data obtained from vapor pressure equilibration, and the few lower magnitude capillary pressure data are directly from the pressure plate measurements. The drainage (desorption) isotherms show that high P_c, generally in the range of ~1 MPa, are need in order to desaturate shales that have been expose to free water. Thus, regions within shale reservoirs that imbibe water-based hydraulic fracturing fluids require substantial water redistribution in order to allow return flow of gas. Given the very low matrix permeabilities of shales, the zones of elevated water saturation can be expected to propagate only short distances beyond fracture surfaces. However, low relative permeabilities also limit rates of water redistribution within matrix pores, thus allowing persistence of water blocks at fracture-matrix boundaries. These results underscore the challenge of moving either the gas phase or water phase through low permeability shales that have been exposed to water, sometimes referred to as the "permeability jail phenomenon" (Shanley et al., 2004; Shaoul et al., 2011).

3.3. Transient Water Vapor Diffusion and Adsorption on Shale

3.3.1. Experimental

Unlike the fairly rapid equilibration of water vapor adsorption measurements on crushed shale grains, measurements on the ~5 mm thick

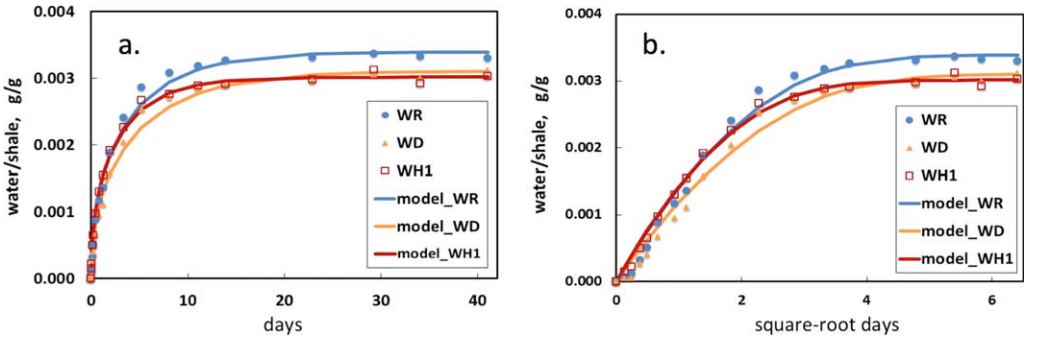

Figure 6. Comparisons between measured and modeled time-dependence of water vapor adsorption onto Woodford Shales continuously exposed to $rh = 0.31$, at 50°C. (a) Water uptake into bulk 5 mm thick samples. (b) Water uptake versus square root of time for the 5 mm thick shale laminae.

shale samples required more than 10 days to achieve equilibrium, reflecting the diffusion-limited nature of the process (Figure 6a). The diffusion-limited approach to adsorption equilibrium is evident from the approximately linear water uptake with respect to the square root of time during the early stages (Figure 6b). It should be noted that these shale laminae are from within the same 0.9 m core depth intervals as their crushed shale counterparts (Tables 1 and 4; and Figures 4 and 5), yet differences among their respective properties resulting from specific positions within the sediment profile are expected. One distinction relative to the crushed shales detected upon XRF scanning of the laminae surfaces was that none of these larger pieces contained elevated levels of Ca (unlike the crushed WH1, Table 4). This may explain the very similar measured levels of water adsorption among the laminae samples (Figure 6), in contrast to the distinctly less hydrophilic behavior of the crushed WH1 shales (Figures 4 and 5).

3.3.2. Modeling

Comparisons between measured water vapor uptake and model results with best fit parameters are shown in Figure 6. Although some discrepancies are evident, especially at very early times, the modeled diffusion with adsorption represents the data reasonably well. Table 6 lists the best fit parameters and the uncertainty in the estimated K_d. The tortuous pore connections and low porosity result in low values of D_{eff}. The estimated values of the D_{eff} are similar for the all three samples. When normalized to D_o from Massman (1998), the bulk gas phase water vapor diffusion coefficient in air, the values are in accord with the porosity-dependence for D_{eff}/D_o values reported in the literature for gas diffusion in low porosity and low permeability rocks (Peng et al., 2012), and solute diffusion in water-saturated low porosity rocks (Boving & Grathwohl, 2001). Thus, despite differences in chemical characteristics, and even differences in phase through which transport occurs (pores saturated with gas versus with aqueous solution), magnitudes of effective diffusion coefficients relative to their values in the bulk fluid phase appear relatively well constrained by porosity.

The nature of the diffusion process becomes evident upon combining the value of $l_o = 110$ nm determined earlier for water vapor diffusion in bulk air at 50°C and 28 kPa, with estimates of representative pore sizes shown along the upper axis in Figure 4. With most of the pore space associated with pore radii ranging from 2 to 5 nm, we see that $Kn = l_o/r_o$ ranges from about 50 to 20. Given such large Kn, water vapor diffusion into shale under our experimental conditions was fully in the Knudsen regime, with individual water molecules colliding primarily with shale pore surfaces. Note that at the much higher total pressures

Table 6
Results of the Model Fitting to the Experimental Data for the Diffusion and Adsorption of Water Molecules in the Shale

	WR	WD	WH1
Porosity	0.081	0.070	0.100
Estimated D_{eff} ($m^2\ s^{-1}$)	1.48×10^{-8}	9.06×10^{-9}	2.78×10^{-8}
D_{eff}/D_o	4.95×10^{-4}	3.03×10^{-4}	9.30×10^{-4}
Estimated K_d ($m^3\ kg^{-1}$)	0.126	0.115	0.112
Standard deviation in estimated K_d ($m^3\ kg^{-1}$)	0.003	0.003	0.001

Note. The D_o value for H_2O-air is from Massman (1998).

associated with gas reservoirs (e.g., 10–30 MPa), l_o becomes substantially smaller, and although simple kinetic theory descriptions such as equation (4) no longer apply. Under the much higher "gas" (supercritical fluid) densities associated with reservoir pressures and temperatures, diffusion is no longer strongly influenced by Knudsen effects. Finally, it should be noted that simplicity of the experimental procedure-limited modeling of bulk H_2O vapor uptake to extracting single (isotropic) values of D_{eff} in each sample, while the shale likely have higher D_{eff} along their bedding plane and low D_{eff} perpendicular to the bedding. The anisotropy of D_{eff} is being examined in ongoing research.

3.4. Conceptual Model Reconciling Water Blocking and Gas Production

The collective evidence from previous studies (Bertoncello et al., 2014; Kamath & Laroche, 2003; Yan et al., 2015) and results presented here indicate that water blocking in unconventional shale reservoirs is very persistent in affected zones. The shale matrix adjacent to water-saturated fractures is expected to become practically water-saturated, with a wetting front that propagates approximately in proportion to the square-root of time (Bell & Cameron, 1906; Birdsell et al., 2015; Green & Ampt, 1911; Roychaudhuri et al., 2013; Tokunaga & Wan, 2001a; Washburn, 1921; Yang et al., 2017). Even though wetting front propagation distances may only extend centimeters beyond fracture surfaces in shales (Birdsell et al., 2015), our measurements showed that $P_c \sim 1$ MPa can be required for significant drainage. This implies that gas production from reservoirs is largely associated with stimulated regions that have had relatively little exposure to injected water such that redistribution of imbibed water occurs quickly. Without efficient displacement of water from a significant fraction of fractures, the very high gas productivity obtained in many unconventional reservoirs appears inconsistent with the practically permanent loss of most of the injected water.

The importance of gravity drainage of water in fractures has been recognized in the context of unsaturated fractured rock hydrology (Faybishenko et al., 2003; Glass, 1993; Nicholl et al., 1994; Tokunaga & Wan, 1997; Tsang & Birkholzer, 1999). Implications of gravity drainage for gas flow in hydraulic fractures were demonstrated in laboratory experiments of Tidwell and Parker (Tidwell & Parker, 1996). Indeed, large fracture apertures ($> 10^{-4}$ m) supported with proppant (Liang et al., 2016) and bounded by very low permeability ($< 10^{-20}$ m^2) matrix surfaces possess a wide range of near-zero P_c where unsaturated drainage of water is efficient (Tokunaga & Wan, 2001b). More recently, gravity drainage has been incorporated in conceptual models for unconventional gas reservoirs (Taylor et al., 2011), and is rapidly gaining recognition (Agrawal & Sharma, 2015; Liu et al., 2017; Parmar et al., 2014; Sarkar et al., 2016). Importantly, time scales for gravity drainage of water from larger fractures are short, thus limiting the volume of water imbibition in regions above horizontal wells to that of the shut-in period. As noted above, imbibition distances into the shale matrix are generally shallow because of their very low permeabilities.

A scenario for water stratification in fractures through gravity drainage is depicted in Figure 1. Similar to the previous depictions cited above, gas (supercritical fluid) flow is sustained in newly formed higher elevation fractures that are quickly gravity-drained into horizontal wells after the shut in period. Adjacent to such drained fractures, very limited volumes of water can be imbibed into matrix pores given the short exposure times. Redistribution of water imbibed into thin saturated zones along the fracture-matrix boundary of the upper zone dissipates the water block and allows gas flow. In contrast, the higher density of water relative to gas acts against drainage of fractures below horizontal wells, and dewatering depends on inefficient water entrainment in gas flow out of fractures and slow water imbibition into the shale matrix (leak-off). Thus, water blocking is envisioned to be more severe in fractures residing below the axes of horizontal wells.

4. Conclusions

The main goal of this study was to obtain a comprehensive set of equilibrium relations for water saturation in shale, spanning a wide range of potential energies in both imbibition and drainage, from which improved understanding of unconventional gas reservoirs can be developed. The measurements on samples of Woodford Shale included basic characterization, adsorption-desorption isotherms, and imbibition-drainage capillary pressure measurements conducted at 50°C. While most of the five shale samples exhibited similar equilibrium hydraulic characteristics, the only calcite-rich sample exhibited less hydrophilic behavior. The fine size of crushed shale samples (~350 and ~700 μm) facilitated rapid equilibration of water contents (typically within 2 days), while larger (~5 mm) shale pieces required long, diffusion-limited equilibration

times (> 10 days). Effective water vapor diffusion coefficients were obtained through modeling of one set of water vapor equilibration experiments conducted at $rh = 0.31$, and were found to range between 9×10^{-9} and 3×10^{-8} m^2 s^{-1}. When normalized to D_o of the bulk fluid phase, these shale D_{eff}/D_o values are similar in magnitude to the values for other low porosity materials. All moisture retention relations exhibited significant hysteresis, and very high capillary pressures on the order of 1 MPa are needed to significantly drain most of the shales that have been exposed to nearly free water (low P_c). Such high drainage P_c and associated water blocking, in combination with loss of most of the water injected during hydraulic fracturing, appear at odds with high rates of gas recovery. Gravity drainage of water in fractures helps reconcile this apparent inconsistency. While water in fractures generated below horizontal wells lack drainage and must largely imbibe into shale matrix pores, gravity facilitates drainage of water back into horizontal wells from newly created overlying fractures, thus allowing gas recovery while minimizing imbibition.

Acknowledgments
This material is based upon work supported by the U.S. Department of Energy, Office of Fossil Energy, Office of Natural Gas and Petroleum Technology, through the National Energy Technology Laboratory (NETL), and Office of Basic Energy Sciences, Chemical Sciences, Geosciences, and Biosciences Division under Award DE-AC02–05CH11231 and FWP-ESD14085. Project management by Stephen Henry (NETL) is gratefully acknowledged. Support for Weijun Shen was provided by the National Science and Technology Major Project of the Ministry of Science and Technology of China Project (50150503-12), and by the Foundation of China Scholarship Council. We thank the Oklahoma Geological Survey and Brian Cardott (OGS) for guidance on sample selection and for Woodford Shale samples, and Wenming Dong (LBNL) for BET measurements. We thank Editor Hari Rajaram, Andreas Busch, and anonymous reviewers for their helpful comments. All data from this study is available in the supporting information.

References

Agrawal, S., & Sharma, M. M. (2015). Practical insights into liquid loading within hydraulic fractures and potential unconventional gas reservoir optimization strategies. *Journal of Unconventional Oil and Gas Resources*, *11*, 60–74.
Alexander, T., Baihly, J., Boyer, C., Clark, B., Waters, G., Jochen, V., . . . Toelle, B. E. (2011). Shale gas revolution. *Oilfield Review*, *23*, 40–55.
Bell, J. M., & Cameron, F. K. (1906). The flow of liquids through capillary spaces. *Journal of Physical Chemistry*, *10*(8), 658–674.
Bennion, D. B., & Thomas, F. B. (2005). Formation damage issues impacting the productivity of low permeability, low initial water saturation gas producing formations. *Journal of Energy Resource Technology*, *127*(3), 240–247.
Bertoncello, A., Wallace, J., Blyton, C., Honarpour, M., & Kabir, C. S. (2014). Imbibition and water blockage in unconventional reservoirs: Well-management implications during flow back and early production. *SPE Reservoir Evaluation & Engineering*, *17*(4), 497–506.
Birdsell, D. T., Rajaram, H., & Lackey, G. (2015). Imbibition of hydraulic fracturing fluids into partially saturated shale. *Water Resources Research*, *51*, 6787–6796. https://doi.org/10.1002/2015WR017621
Boving, T. B., & Grathwohl, P. (2001). Tracer diffusion coefficients in sedimentary rocks: Correlation to porosity and hydraulic conductivity. *Journal of Contaminant Hydrology*, *53*(1–2), 85–100.
Brunauer, S., Emmett, P. H., & Teller, E. (1938). Adsorption of gases in multimolecular layers. *Journal of the American Chemical Society*, *60*, 309–319.
Busch, A., & Amann-Hildenbrand, A. (2013). Predicting capillarity of mudrocks. *Marine and Petroleum Geology*, *45*, 208–223.
Cardott, B. J. (2012). Thermal maturity of Woodford Shale gas and oil plays, Oklahoma, USA. *International Journal of Coal Geology*, *103*, 109–119.
Chenevert, M. E. (1970). Shale alteration by water adsorption. *Journal of Petroleum Technology*, *22*, 1141–1148.
Clark, C. E., Horner, R. M., & Harto, C. B. (2013). Life cycle water consumption for shale gas and conventional natural gas. *Environmental Science & Technology*, *47*(20), 11829–11836.
Clarkson, C. R., Solano, N., Bustin, R. M., Bustin, A. M. M., Chalmers, G. R. L., Le, L., . . .Blach, T. P. (2013). Pore structure characterization of North American shale gas reservoirs using USANS/SANS, gas adsorption, and mercury intrusion. *Fuel*, *103*, 606–616.
Dane, J. H., & Hopmans, J. W. (2002). Pressure plate extractor. In J. H. Dane & G. C. Topp (Eds.), *Methods of soil analysis, part 4: Physical methods* (pp. 688–690). Madison, WI: Soil Science Society America.
Dehghanpour, H., Lan, Q., Saeed, Y., Fei, H., & Qi, Z. (2013). Spontaneous imbibition of brine and oil in gas shales: Effect of water adsorption and resulting microfractures. *Energy and Fuels*, *27*(6), 3039–3049.
Donnelly, B., Perfect, E., McKay, L. D., Lemiszki, P. J., DiStefano, V. H., Anovitz, L. M., . . .Cheng, C.-L. (2016). Capillary pressure: Saturation relationships for gas shales measured using a water activity meter. *Journal of Natural Gas Science and Engineering*, *33*, 1342–1352.
Dosunmu, A., & Okoro, E. E. (2012). Determination of moisture adsorption isotherm of shale from Agbada Formation using GAB model. *Research Journal of Engineering Sciences*, *1*(4), 27–33.
Downs, R. T., & Hall-Wallace, M. (2003). The American Mineralogist crystal structure database. *American Mineralogist*, *88*(1), 247–250.
Elgmati, M., Zhang, H., Bai, B., Flori, R., & Qu, Q. (2011). *Submicron-pore characterization of shale gas plays*. Paper SPE 144050 presented at SPE North American Unconventional Gas Conference and Exhibition (p. 19). Society of Petroleum Engineers, The Woodlands, TX. https://doi.org/10.2118/144050-MS
Engelder, T., Cathles, L. M., & Bryndzia, L. T. (2014). The fate of residual treatment water in gas shale. *Journal of Unconventional Oil and Gas Resources*, *7*, 33–48.
EPA (2016). *Hydraulic fracturing for oil and gas: Impacts from hydraulic fracturing water cycle on drink water resources in the United States* (50 pp.). Washington, DC: United States Environmental Protection Agency.
Faybishenko, B., Bodvarsson, G. S., & Salve, R. (2003). On the physics of unstable infiltration, seepage, and gravity drainage in partially saturated tuffs. *Journal of Contaminant Hydrology*, *62–3*, 63–87.
Ferrari, A., Favero, V., Marschall, P., & Laloui, L. (2014). Experimental analysis of the water retention behaviour of shales. *International Journal of Rock Mechanics and Mining Sciences*, *72*, 61–70.
Finsterle, S., & Zhang, Y. Q. (2011). Solving iTOUGH2 simulation and optimization problems using the PEST protocol. *Environmental Modelling & Software*, *26*(7), 959–968.
Fisher, L. R., & Israelachvili, J. N. (1979). Direct experimental verification of the Kelvin equation for capillary condensation. *Nature*, *277*(5697), 548–549.
Gallegos, T. J., Varela, B. A., Haines, S. S., & Engle, M. A. (2015). Hydraulic fracturing water use variability in the United States and potential environmental implications. *Water Resources Research*, *51*, 5839–5845. https://doi.org/10.1002/2015WR017278
Glass, R. J. (1993, April 26–30). *Modeling gravity-driven fingering in rough-walled fractures using modified percolation theory*. Paper presented at Proceedings of the Fourth Annual International Conference. High Level Radioactive Waste Management. American Society of Civil Engineers, ANS, Las Vegas, NV.
Green, W. H., & Ampt, G. A. (1911). Studies on soil physics Part I: The flow of air and water through soils. *Journal of Agricultural Science*, *4*, 1–24.
Greenspan, L. (1977). Humidity fixed-points of binary saturated aqueous solutions. *Journal of Research National Bureau of Standards—A: Physics and Chemistry*, *81*(1), 89–96.

Gupta, D. V. S. (2009). *Unconventional fracturing fluids for tight gas reservoirs*. Paper SPE 119424 presented at SPE Hydraulic Fracturing Technology Conference (p. 9). Society of Petroleum Engineers, The Woodlands, TX. https://doi.org/10.2118/119424-MS

Gupta, D. V. S., & Bobier, D. M. (1998). *The history and success of liquid CO2 and CO2/N2 fracturing systems*. Paper SPE 40016-MS presented at SPE Gas Technology Symposium (p. 8). Society of Petroleum Engineers, Calgary, AL. https://doi.org/10.2118/40016-MS

Holditch, S. A. (1979). Factors affecting water blocking and gas-flow from hydraulically fractured gas-wells. *Journal of Petroleum Technology*, *31*(12), 1515–1524.

Kamath, J., & Laroche, C. (2003). Laboratory-based evaluation of gas well deliverability loss caused by water blocking. *SPE Journal*, *8*(1), 71–80.

Krishna, R., & Wesselingh, J. A. (1997). Review article number 50: The Maxwell-Stefan approach to mass transfer. *Chemical Engineering Science*, *52*(6), 861–911.

Kuila, U., & Prasad, M. (2013). Specific surface area and pore-size distribution in clays and shales. *Geophysical Prospecting*, *61*(2), 341–362.

Li, J., Li, X., Wang, X., Li, Y., Wu, K., Shi, J., . . . Yu, P. (2016). Water distribution characteristic and effect on methane adsorption capacity in shale clay. *International Journal of Coal Geology*, *159*, 135–154.

Li, J. R., Kuppler, R. J., & Zhou, H. C. (2009). Selective gas adsorption and separation in metal-organic frameworks. *Chemical Society Reviews*, *38*(5), 1477–1504.

Liang, F., Sayed, M., Al-Muntasheri, G. A., & Chang, F. F. (2016). A comprehensive review on proppant technologies. *Petroleum*, *2*, 26–39.

Liu, H., Wang, F., Zhang, J., Meng, S. W., & Duan, Y. W. (2014). Fracturing with carbon dioxide: Application status and development trend. *Petroleum Exploration and Development*, *41*(4), 513–519.

Liu, Y., Leung, J. Y., Chalaturnyk, R., & Virues, C. J. J. (2017). *Fracture fluid distribution in shale gas reservoirs due to fracture closure, proppant distribution, and gravity segregation*. Paper SPE-185043-MS presented at SPE Unconventional Resources Conference (p. 21). Society of Petroleum Engineers, Calgary, AL. https://doi.org/10.2118/185043-MS

Loeb, L. B. (1961). *The kinetic theory of gases* (3rd ed.). New York, NY: Dover Publications Inc.

Massman, W. J. (1998). A review of the molecular diffusivities of H2O, CO2, CH4, CO, O-3, SO2, NH3, N2O, NO, AND NO2 in air, O-2 AND N-2 near STP. *Atmospheric Environment*, *32*(6), 1111–1127.

Mitropoulos, A. C. (2008). The Kelvin equation. *Journal of Colloid and Interface Science*, *317*(2), 643–648.

Morrow, N. R. (1990). Wettability and its effect on oil-recovery. *Journal of Petroleum Technology*, *42*(12), 1476–1484.

Nelson, P. H. (2009). Pore-throat sizes in sandstones, tight sandstones, and shales. *AAPG Bulletin*, *93*(3), 329–340.

Nicholl, M. J., Glass, R. J., & Wheatcraft, S. W. (1994). Gravity-driven infiltration instability in initially dry nonhorizontal fractures. *Water Resources Research*, *30*(9), 2533–2546.

Ozisik, M. N. (1980). *Heat conduction*. New York, NY: John Wiley.

Parmar, J., Dehghanpour, H., & Kuru, E. (2014). Displacement of water by gas in propped fractures: Combined effects of gravity, surface tension, and wettability. *Journal of Unconventional Oil and Gas Resources*, *5*, 10–21.

Peng, S., Hu, Q. H., & Hamamoto, S. (2012). Diffusivity of rocks: Gas diffusion measurements and correlation to porosity and pore size distribution. *Water Resources Research*, *48*, W02507. https://doi.org/10.1029/2011WR011098

Pollard, W. G., & Present, R. D. (1948). On gaseous self-diffusion in long capillary tubes. *Physical Review*, *73*(7), 762–774.

Quirk, J. P. (1955). Significance of surface areas calculated from water vapor sorption isotherms by use of the B.E.T. equation. *Soil Science*, *80*(6), 423–430.

Ross, D. J. K., & Bustin, R. M. (2009). The importance of shale composition and pore structure upon gas storage potential of shale gas reservoirs. *Marine and Petroleum Geology*, *26*(6), 916–927.

Rouquerol, J., Avnir, D., Everett, D. H., Fairbridge, C., Haynes, M., Pernicone, N., . . .Unger, K. K. (1994). Recommendations for the characterization of porous solids. *Pure and Applied Chemistry*, *66*(8), 1739–1758.

Roychaudhuri, B., Tsotsis, T. T., & Jessen, K. (2013). An experimental investigation of spontaneous imbibition in gas shales. *Journal of Petroleum Science and Engineering*, *111*, 87–97.

Sarkar, S., Haghighi, M., Sayyafzadeh, M., Cooke, D., Pokalai, K., & Ali Sahib, F. M. (2016). A Cooper Basin simulation study of flow-back after hydraulic fracturing in tight gas wells. *APPEA Journal*, 369–392.

Schmitt, L., Forsans, T., & Santarelli, F. J. (1994). Shale testing and capillary phenomena. *International Journal of Rock Mechanics and Mining Sciences & Geomechanics Abstracts*, *31*(5), 411–427.

Seemann, T., Bertier, P., Krooss, B. M., Stanjek, H. (2017). Water vapor sorption on mudrocks. In E. H. Rutter (Ed.), *Geomechanical and petrophysical properties of mudrocks* (p. 33). London, UK: Geological Society of London.

Shanley, K. W., Cluff, R. M., & Robinson, J. W. (2004). Factors controlling prolific gas production from low-permeability sandstone reservoirs: Implications for resource assessment, prospect development, and risk analysis. *AAPG Bulletin*, *88*(8), 1083–1121.

Shaoul, J., van Zelm, L., & de Pater, C. J. (2011). Damage mechanisms in unconventional-gas-well stimulation-A new look at an old problem. *SPE Production and Operation*, *26*(4), 388–400.

Sing, K. S. W., & Williams, R. T. (2004). Physisorption hysteresis loops and the characterization of nanoporous materials. *Adsorption Science & Technology*, *22*(10), 773–782.

Singh, H. (2016). A critical review of water uptake by shales. *Journal of Natural Gas Science and Engineering*, *34*, 751–766.

Spencer, C. W. (1989). Review of characteristics of low-permeability gas-reservoirs in Western United-States. *AAPG Bulletin*, *73*(5), 613–629.

Sposito, G. (1981). *The thermodynamics of soil solutions* (223. pp.). Oxford, UK: Oxford University Press.

Sposito, G. (1984). *The surface chemistry of soils* (234. pp.). New York, NY: Oxford University Press.

Taylor, R. S., Barree, R., Aguilera, R., Hoch, O., & Storozhenko, K. (2011). *Why not to base economic evaluations on initial production alone*. Paper SPE-148680-MS presented at Canadian Unconventional Resources Conference. Society of Petroleum Engineers, Calgary, AL. https://doi.org/10.2118/148680-MS

Tidwell, V., & Parker, M. (1996). *Laboratory imaging of stimulation fluid displacement from hydraulic fractures*. Paper SPE-36491-MS presented at SPE Annual Technical Conference and Exhibition (pp. 793–804). Society of Petroleum Engineers, Denver, CO. https://doi.org/10.2118/36491-MS

Tokunaga, T. K. (1985). Porous media gas diffusivity from a free-path distribution model. *Journal of Chemical Physics*, *82*(11), 5298–5299.

Tokunaga, T. K., Olson, K. R., & Wan, J. (2003). Moisture characteristics of Hanford gravels: Bulk, grain-surface, and intragranular components. *Vadose Zone Journal*, *2*(3), 322–329.

Tokunaga, T. K., & Wan, J. (1997). Water film flow along fracture surfaces of porous rock. *Water Resources Research*, *33*(6), 1287–1295.

Tokunaga, T. K., & Wan, J. (2001a). Surface-zone flow along unsaturated rock fractures. *Water Resources Research*, *37*(2), 287–296.

Tokunaga, T. K., & Wan, J. (2001b). Approximate boundaries between different flow regimes in fractured rocks. *Water Resources Research*, *37*(8), 2103–2111.

Tsang, Y. W., & Birkholzer, J. T. (1999). Predictions and observations of the thermal-hydrological conditions in the Single heater test. *Journal of Contaminant Hydrology*, *38*(1–3), 385–425.

Vengosh, A., Jackson, R. B., Warner, N., Darrah, T. H., & Kondash, A. (2014). A critical review of the risks to water resources from unconventional shale gas development and hydraulic fracturing in the United States. *Environmental Science & Technology*, *48*(15), 8334–8348.

Wanniarachchi, W. A. M., Ranjith, P. G., & Perera, M. S. A. (2017). Shale gas fracturing using foam-based fracturing fluid: A review. *Environmental Earth Sciences*, *76*(2),

Washburn, E. W. (1921). The dynamics of capillary flow. *Physical Review*, *17*(3), 273–283.

Wesselingh, J. A., & Krishna, R. (2000). Mass transfer in multicomponent mixtures. Delft, the Netherlands: VSSD.

Xue, Z., Worthen, A. J., Da, C., Qajar, A., Ketchum, I. R., Alzobaidi, S., . . . Johnston, K. P. (2016). Ultradry carbon dioxide-in-water foams with viscoelastic aqueous phases. *Langmuir*, *32*(1), 28–37.

Yan, Q., Lemanski, C., Karpyn, Z. T., & Ayala, L. F. (2015). Experimental investigation of shale gas production impairment due to fracturing fluid migration during shut-in time. *Journal of Natural Gas Science and Engineering*, *24*, 99–105.

Yang, R., Guo, X. S., Yi, J. Z., Fang, Z. X., Hu, Q. H., & He, S. (2017). Spontaneous imbibition of three leading shale formations in the Middle Yangtze Platform, South China. *Energy and Fuels*, *31*(7), 6903–6916.